Reconstructive Elasticity Imaging for Large Deformations

Andrei R. Skovoroda, Mark A. Lubinski, *Student Member, IEEE*, Stanislav Y. Emelianov, *Member, IEEE*, and Matthew O'Donnell, *Fellow, IEEE*

***Abstract*—A method is presented to reconstruct the elastic modulus of soft tissue based on ultrasonic displacement and strain images for comparatively large deformations. If the average deformation is too large to be described with a linear elastic model, nonlinear displacement-strain relations must be used and the mechanical equilibrium equations must include high order spatial derivatives of the displacement. Numerical methods were developed to reduce error propagation in reconstruction algorithms, including these higher order derivatives. Problems arising with the methods, as well as results using ultrasound measurements on gel-based, tissue equivalent phantoms, are given. Comparison to reconstructions using a linear elastic model shows that equivalent image quality can be produced with algorithms appropriate for finite amplitude deformations.**

I. Introduction

IMAGES of mechanical displacements and strains within soft tissue present information about the elasticity of internal structures [1]–[21]. Interpreting these images, however, can be difficult for complex mechanical objects such as soft tissue. To potentially simplify image interpretation and reduce artifacts due solely to object geometry, several investigators have explored elastic modulus reconstruction [9], [10], [17], [22]. Exact reconstruction is impossible without detailed knowledge of the mechanical boundary conditions (i.e., the Young's modulus needs to be specified along some boundary, as discussed later in this paper). Nevertheless, methods have been developed to produce relative reconstructions, even if detailed mechanical boundary conditions are unknown [9], [10].

Previous work from our laboratories has shown that the Young's (or equivalently the shear) modulus of soft tissue and tissue-like phantoms can be reconstructed from mechanical displacement and strain images acquired during static external deformation [5]–[10], [12], [18]–[21]. Different imaging systems (e.g., ultrasound and MRI), as well as different deformation procedures, were used to generate displacement and strain images. Consequently, effective numerical methods were developed for all systems to reconstruct the relative Young's modulus based on a linear elastic model. These techniques do not require any information about global boundary conditions (i.e., mechanical constraint of the body, its geometry, the types of external and internal forces, etc. [9]). In principle, however, they are limited to low magnitude external deformations in which a linear model is valid. Here we extend these methods to finite amplitude deformations.

Large external deformations increase the signal-to-noise ratio (SNR) of displacement and strain images [5]–[10], [23]. Unfortunately, large deformations of soft tissue and tissue-like materials cannot be described with a linear elastic model. A linear model can break down in two ways. First, for most soft tissues, the elastic modulus increases as a function of strain (i.e., strain hardening). This effect is often referred to as "material nonlinearity." Second, a more complete description of the equilibrium equation, including nonlinear strain-displacement relations, must be used for large deformations. This effect is often referred to as "geometric nonlinearity." Due to the high order displacement derivatives resulting from this description, error propagation must be minimized in any reconstruction algorithm using measured displacement data with a finite signal to noise ratio.

In this paper, we examine the second form of nonlinearity, namely, geometric nonlinearities arising from large amplitude deformations. These studies were conducted on gelatin phantoms with almost no material nonlinearities over the deformation range considered here (average strain up to 14%). Material nonlinearities in soft tissue are considered in [24], [25]. The specific purpose of the present study was to explore numerical methods minimizing the effects of higher order displacement derivatives needed to describe finite amplitude deformations on elasticity reconstruction.

Previous algorithms for elasticity reconstruction were formulated using the set of equations describing mechanical equilibrium in a statically deformed, linear elastic medium [5], [9], [10], [18]–[21], [24], [26]. Independent of the specific elastic model, however, these equations can be posed in either differential or integral form. An integral representation is more appropriate for a nonlinear model given realistic measurement noise. As discussed in Section II, numerical methods have been developed for both linear and nonlinear models exploiting an integral representation of the reconstruction equations. The specific approach assumes a plane strain state to approximate two-

Manuscript received September 18, 1997; accepted November 12, 1998. Support from the National Institutes of Health under Grant DK 47324 and from US Army under Grant DAMD17-97-7079 is gratefully acknowledged.

A. R. Skovoroda and S. Y. Emelianov are with the Institute of Mathematical Problems of Biology, Russian Academy of Sciences, Pushchino, Russia 142292.

M. A. Lubinski, S. Y. Emelianov, and M. O'Donnell are with the Electrical Engineering and Computer Science and Biomedical Engineering Departments, University of Michigan, Ann Arbor, MI 48109-2125.

dimensional displacement and strain images obtained with a real-time ultrasound scanner. The full three-dimensional problem is discussed in the Appendix.

Displacement data acquired with a real-time ultrasound scanner were used to test the numerical methods of Section II. Relative elastic modulus images were reconstructed within a gel-based, tissue equivalent phantom with prescribed mechanical properties using both linear and nonlinear models. Methods for displacement and strain image acquisition are presented in Section III. All results are presented in Section IV. The paper concludes with a discussion of the results in Section V.

II. Theory

Consider a three-dimensional (3-D) volume V of deformed media with the displacement vector $U = U(x_1, x_2, x_3) = (u_1, u_2, u_3)$ in Cartesian coordinates x_i, $i = 1, 2, 3$. The volume V can be either the entire mechanical body or a region of interest inside the object.

The most general nonlinear mechanical equilibrium equations are [27]–[31].

$$\sum_{j=1}^{2} \left\{ \sum_{n=1}^{3} [\sigma_{nj}(\delta_{in} + u_{i,n})] \right\}_{,j} = 0 \quad i = 1, 2, 3. \tag{1}$$

Here σ_{nj} is a component of the 2nd ranked stress tensor and δ_{in} is the Kronecker delta symbol. In (1), and the rest of this paper, the lower index after a comma means differentiation with respect to the corresponding spatial Lagrangian coordinate. Note that spatial coordinates and displacement components correspond to the initial, not deformed, configuration of the object under investigation. Similarly, all images are presented in the original object geometry (i.e., before deformation).

Equation (1) must be satisfied at every internal point of the body. If the magnitudes of the spatial derivatives of all displacement components are small, the last terms $u_{i,n}$ in (1) can be omitted, producing the familiar linear equilibrium equations [32], [33]:

$$\sum_{j=1}^{3} \sigma_{ij,j} = 0, \quad i = 1, 2, 3. \tag{2}$$

To complete the system of equations describing internal deformations, the relation between stress and strain tensors, as well as the relation between the strain tensor and the displacement vector, are needed. Here we assume that the standard linear relation between the stress tensor σ_{ij} and the strain tensor ε_{ij} for incompressible media is still valid [27]–[34]:

$$\sigma_{ij} = p\delta_{ij} + 2\mu\varepsilon_{ij}, \tag{3}$$

where p is the static, internal pressure and the shear elastic modulus μ is considered a constant independent of the strain magnitude. Computing the spatial distribution of the shear elastic modulus is the goal of reconstruction. Note in an incompressible material, such as soft tissue, the shear and Young's moduli are simply proportional (i.e., $E = \mu/3$). Thus, shear modulus and Young's modulus reconstructions are equivalent.

In the following derivation we assume a plane strain state in which spatial derivatives of the out-of-plane displacement u_3 are either zero or small compared to the others, and the two in-plane components u_1 and u_2 do not vary significantly as functions of the out-of-plane coordinate [5], [6], [8], [10], [12], [18], [19], [21], [32]. Nonlinear elasticity reconstruction for a general three-dimensional strain state is considered and discussed in the Appendix.

Because the pressure p cannot be directly measured with an imaging system, it must be eliminated from the equations describing mechanical equilibrium [5], [9], [10], [18]–[22], [26]. For the linear case, eliminating p from (2) and (3) leads to a partial differential equation for the unknown shear elasticity distribution $\mu = \mu(x, y)$:

$$(\mu\varepsilon_{xy})_{,xx} - (\mu\varepsilon_{xy})_{,yy} + 2(\mu\varepsilon_{yy})_{,xy} = 0, \tag{4}$$

where the spatial coordinates x_1 and x_2 are denoted here by x and y. Note that the incompressibility condition, $\varepsilon_{11} + \varepsilon_{22} = 0$, is used to produce the specific form presented in (4). All strains in this equation are defined by the linear strain-displacement relation:

$$\varepsilon_{ij}^{\text{lin}} = \frac{1}{2}(u_{i,j} + u_{j,i}). \tag{5}$$

The reconstruction procedure assumes that all relevant displacements are known (i.e., measured), and solves for the shear elasticity distribution satisfying both (4) and the mechanical boundary conditions.

Except for the degenerate (i.e., parabolic) case corresponding to an in-plane translation with rotation of the volume as a rigid body, internal deformations are described by a hyperbolic, 2nd order differential equation [9], [26]. This means there is a unique shear modulus distribution satisfying (4) given appropriate mechanical boundary conditions. Rather than specifying displacement and stress values at the object boundary [17], a much simpler boundary value problem can be formulated using the method of characteristics in which the modulus, and/or spatial derivatives of the modulus are specified solely along a set of characteristic curves (see [35], Chapter 10). For the differential equation given in (4), these curves are defined by all points (x, y) satisfying the following relation:

$$\varepsilon_{xy}dy = \left(\varepsilon_{yy} \pm \sqrt{\varepsilon_{yy}^2 + \varepsilon_{xy}^2}\right) dx. \tag{6}$$

To illustrate how the characteristic curves of (4) help formulate elasticity reconstruction as a simplified boundary value problem, deformation data (i.e., all components of the strain tensor) from an inhomogeneous gel-based tissue equivalent phantom were analyzed. These data were collected using the methods described in Section III. The characteristic curves computed according to (6) over a 25-mm by 65-mm area within the phantom are presented in

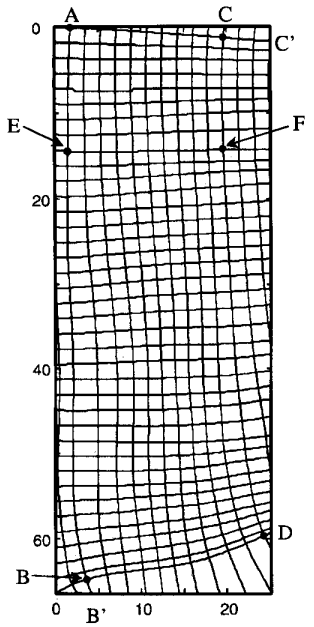

Fig. 1. Characteristic curves of (6) computed from ultrasound measurements on the inhomogeneous gel-based phantom.

Fig. 1. Displayed here are all characteristics starting at the bottom and left side of the region at equal (approximately 1.8 mm) intervals. If, for example, the distribution $\mu(x,y)$ is given along parts AB and AC of two intersecting characteristics AB' and AC', then the reconstruction for region $ABDC$ reduces to a classic Goursat boundary problem for (4). In contrast, to get the unique solution of (4) within the region CEF, the values of μ, $\partial\mu/\partial x$, and $\partial\mu/\partial y$ must be prescribed along the single line CE (see [35], Chapter 10).

In this paper we only consider reconstruction based on two intersecting characteristic curves defining a region of interest (ROI). If the exact value of the elastic modulus is not known along these two curves, reconstruction within the ROI is relative. That is, the reconstructed modulus is normalized to the value along the intersecting characteristics. Because the primary goal of reconstruction is artifact reduction rather than exact quantitation, a relative modulus image is sufficient. As discussed in [9], regions of nearly constant elastic modulus can be identified with edge detection operators acting on strain images.

Using the characteristic curves, numerical methods can be developed to solve (4) given displacement measurements. In practice, however, the problem of elasticity reconstruction is greatly complicated even in the linear case due to noisy displacement measurements (i.e., due to noisy coefficients in (4)) and propagation of this noise through numerical integration within the ROI. Therefore, a specific procedure to integrate (4) across the ROI must be used [5], [8]–[10], [12], [18]–[21].

To produce a more stable reconstruction procedure appropriate for noisy deformation data, substitute (3) into (2) and integrate rather than differentiate. After eliminating the unknown pressure, the system of equations reduces to an integral equation of the form:

$$\delta(x,y) \equiv 4\left[\varepsilon_{yy}\mu - (\varepsilon_{yy}\mu)|_{x_0} - (\varepsilon_{yy}\mu)|_{x_0,y_0}\right] + \int_{y_0}^{y} \left[(\gamma\mu)_{,x} - \{(\gamma\mu)_{,x}\}|_{x_0}\right] dy - \int_{x_0}^{x} \left[(\gamma\mu)_{,y} - \{(\gamma\mu)_{,y}\}|_{y_0}\right] dx = 0, \quad (7)$$

where $\gamma = 2\varepsilon_{xy}$ and the notations $f|_{x0} = f(x_0,y)$ and $f|_{y0} = f(x,y_0)$ are used in this equation and below.

The integral equation in (7) is expressed as a functional $\delta(x,y)$, as the goal of reconstruction with noisy data will be to force $\delta(x,y)$ to approach zero in some average sense across the ROI. In contrast with (4), this equation does not contain second order derivatives of the strain. Moreover, the shear strain, and spatial derivatives of the shear strain, only appear in the integral terms. Because noisy lateral displacement estimates only contribute to the shear strain, the effects of measurement error will be reduced by the smoothing action of the integral without sacrificing spatial resolution [36]. This type of processing is similar to incompressibility methods in which noisy lateral displacement measurements are smoothed by integrating higher SNR axial strains without losing spatial resolution [37], [38]. Therefore, elasticity reconstruction by (7) should be more stable.

For large deformations, a similar functional must be defined from the general equilibrium equations of (1) and the general Lagrangian strain-displacement relation. Denoting the displacement components u_1 and u_2 by u and v, the unwrapped form of (1) for the plane strain state is:

$$\begin{aligned}(\sigma_{xx,x} + \sigma_{xy,y})(1+u_{,x}) + (\sigma_{xx}u_{,xx} + \sigma_{yy}u_{,yy}) \\ +(\sigma_{xy,x} + \sigma_{yy,y})u_{,y} + 2\sigma_{xy}u_{,xy} = 0 \\ (\sigma_{xy,x} + \sigma_{yy,y})(1+v_{,y}) + (\sigma_{xx}v_{,xx} + \sigma_{yy}v_{,yy}) \\ +(\sigma_{xx,x} + \sigma_{xy,y})v_{,x} + 2\sigma_{xy}v_{,xy} = 0.\end{aligned} \quad (8)$$

By incorporating the stress-strain relation (3) into (8) and rearranging terms, the following linear system of equations for derivatives of the unknown static internal pressure, $p_{,x}$ and $p_{,y}$, results:

$$A\nabla(p) = -pB - F, \quad (9)$$

where

$$A(x,y) = \begin{pmatrix} 1+u_{,x} & u_{,y} \\ v_{,x} & 1+v_{,y} \end{pmatrix}, \quad B(x,y) = (b_i) = \nabla^2 U,$$

$$F = (f_i),\ i = 1,2;$$

$$\nabla = (\partial/\partial x, \partial/\partial y), \quad \nabla^2 = \partial^2/\partial x^2 + \partial^2/\partial y^2;$$

$$\begin{aligned} f_1 &= 2[(1+u_{,x})\psi_1 + u_{,y}\psi_2 \\ &\quad + (\varepsilon_{xx}u_{,xx} + \varepsilon_{yy}u_{,yy} + 2\varepsilon_{xy}u_{,xy})\mu], \\ f_2 &= 2[v_{,x}\psi_1 + (1+v_{,y})\psi_2 \\ &\quad + (\varepsilon_{xx}v_{,xx} + \varepsilon_{yy}v_{,yy} + 2\varepsilon_{xy}v_{,xy})\mu], \end{aligned}$$

$$\psi_1 = (\mu\varepsilon_{xx})_{,x} + (\mu\varepsilon_{xy})_{,y} \quad \psi_2 = (\mu\varepsilon_{xy})_{,x} + (\mu\varepsilon_{yy})_{,y}.$$

These formulas contain the components of the nonlinear Lagrangian strain tensor [27]–[31]:

$$\varepsilon_{ij} = \frac{1}{2}\left(u_{i,j} + u_{j,i} + \sum_k u_{k,i}u_{k,j}\right). \tag{10}$$

For a plane strain state, the strain tensor components take the specific form:

$$\begin{aligned}\varepsilon_{xx} &= u_{,x} + [(u_{,x})^2 + (v_{,x})^2]/2,\\ \varepsilon_{yy} &= v_{,y} + [(u_{,y})^2 + (v_{,y})^2]/2,\\ \varepsilon_{xy} &= [u_{,y} + v_{,x} + u_{,x}u_{,y} + v_{,x}v_{,y}]/2.\end{aligned} \tag{11}$$

If the magnitudes of the spatial derivatives of all displacement components are small, the last (nonlinear) term in (10) can be omitted to produce the linear strain tensor of (5).

Again, the unknown pressure must be removed from (9). To do this, we solve (9) with respect to unknowns $p_{,x}$ and $p_{,y}$:

$$\nabla(p) = \alpha p + \beta, \tag{12}$$

where $\alpha(x,y) = (\alpha_i) = -A^{-1}B$, $\beta(x,y) = (\beta_i) = -A^{-1}F$, $i = 1, 2$. Then, integrating the first of these equations along x and the second along y, two simultaneous expressions for the unknown pressure are produced:

$$p(x,y) = \varphi_1\left[p(x_0,y) + \int_{x_0}^{x}\frac{\beta_1}{\varphi_1}dx\right] \tag{13.1}$$

$$p(x,y) = \varphi_2\left[p(x,y_0) + \int_{y_0}^{y}\frac{\beta_2}{\varphi_2}dy\right], \tag{13.2}$$

where $\varphi_1(x,y) = \exp\left\{\int_{x_0}^{x}\alpha_1(x,y)dx\right\}$ and $\varphi_2(x,y) = \exp\left\{\int_{y_0}^{y}\alpha_2(x,y)dy\right\}$ do not depend on $\mu(x,y)$. The term $p(x,y_0)$ in (13.2) can be obtained from (13.1). Similarly, the $p(x_0,y)$ in (13.1) can be obtained from (13.2). Consequently, the set of simultaneous equations describing the unknown pressure reduces to a single equation,

$$\begin{aligned}\varphi_1\int_{x_0}^{x}\frac{\beta_1}{\varphi_1}dx - \varphi_2\left[\varphi_1\int_{x_0}^{x}\frac{\beta_1}{\varphi_1}dx\right]\Bigg|_{y_0} - \varphi_2\int_{y_0}^{y}\frac{\beta_2}{\varphi_2}dy\\ + \varphi_1\left[\varphi_2\int_{y_0}^{y}\frac{\beta_2}{\varphi_2}dy\right]\Bigg|_{x_0} - Gp_0 = 0,\end{aligned} \tag{14}$$

where $G(x,y) = [\varphi_2(x,y)\varphi_1(x,y_0) - \varphi_1(x,y)\varphi_2(x_0,y)]$ does not depend on $\mu(x,y)$, and $p_0 = p(x_0,y_0)$.

The expression given in (14) can be used to reconstruct the shear modulus given large deformations. Before defining a functional similar to (7) for the nonlinear case, we consider a simplification of the matrix A^{-1} based on an assumption of incompressibility. The matrix A^{-1} is defined as:

$$A^{-1} = \frac{\begin{pmatrix}1+v_{,y} & -u_{,y}\\ -v_{,x} & 1+u_{,x}\end{pmatrix}}{\det(A)}. \tag{15}$$

The determinant of A is simply related to the metric tensor:

$$\det(A) = 1 + (u_{,x} + v_{,y}) + (u_{,x}v_{,y} - v_{,x}u_{,y}) = \sqrt{g}, \tag{16}$$

where $g = \det(g_{ij})$ is the determinant of the 2nd ranked metric tensor g_{ij}.

The density ρ of a deformed medium is related to the density ρ_0 of the undeformed medium by [29], [37]:

$$\rho = \rho_0/\sqrt{g}. \tag{17}$$

For incompressible materials $g = 1$, and $\det(A) = 1$. Therefore, (15) reduces to:

$$A^{-1} = \begin{pmatrix}1+v_{,y} & -u_{,y}\\ -v_{,x} & 1+u_{,x}\end{pmatrix}. \tag{18}$$

Substituting (18) into (14) and integrating, we obtain an expression for the reconstruction functional in the nonlinear case, as seen in (19) (top of next page), where

$$\begin{aligned}\varepsilon &= \varepsilon_{yy} - \varepsilon_{xx}, \quad \gamma = 2\varepsilon_{xy},\\ g_1 &= 2\{\varepsilon[u_{,yy}(1+v_{,y}) - v_{,yy}u_{,y}]\\ &\quad + \gamma[u_{,xy}(1+v_{,y}) - v_{,xy}u_{,y}\},\\ g_2 &= 2\{-\varepsilon[v_{,xx}(1+u_{,x}) - u_{,xx}v_{,x}]\\ &\quad + \gamma[v_{,xy}(1+u_{,x}) - u_{,xy}v_{,x}\}.\end{aligned}$$

In the limit of small displacements, $\alpha = 0$, $\varphi_i \equiv 1$, $i = 1, 2$, $G(x,y) \equiv 0$, and all second order terms in g_i can be ignored. For this case, (19) reduces to (7). Consequently, (19) can be used as the reconstruction functional over a wide range of internal deformations. In contrast to (4), the differential equation for the nonlinear case after eliminating p contains 4th order displacement derivatives. Therefore, an integral representation for the nonlinear case is also much more appropriate given realistic measurement noise.

To evaluate either (7) or (19), spatial derivatives of both the axial and lateral displacement components are needed. It is well known, however, that lateral displacement measurements are much noisier than axial ones if ultrasound is used to track internal deformations [7], [37], [38]. In addition to smoothing from the integral representation of the equilibrium equation, incompressibility processing can be used in both linear and nonlinear cases to further reduce the influence of noisy displacement measurements [37], [38]. All results presented in Section III used lateral displacement estimates obtained from incompressibility processing.

To solve for the unknown shear elasticity distribution $\mu(x,y)$ given all measured displacements and strains

$$\delta(x,y) \equiv 2\left\{\varepsilon\mu - [\varepsilon\mu + (\varepsilon_{xx}\mu)|_{x_0}\varphi_1]\Big|_{y_0}\varphi_2 - [\varepsilon\mu - (\varepsilon_{yy}\mu)|_{y_0}\varphi_2]\Big|_{x_0}\varphi_1\right\} + \left\{\int_{y_0}^{y}[(\gamma\mu)_{,x} + \mu g_2]\varphi_2^{-1}dy\right\}\varphi_2 - \left\{\varphi_2\int_{y_0}^{y}[(\gamma\mu)_{,x} + \mu g_2]\varphi_2^{-1}dy\right\}\Bigg|_{x_0}\varphi_1 - \left\{\int_{x_0}^{x}[(\gamma\mu)_{,y} + \mu g_1]\varphi_1^{-1}dx\right\}\varphi_1 - \left\{\varphi_1\int_{x_0}^{x}[(\gamma\mu)_{,y} + \mu g_1]\varphi_1^{-1}dx\right\}\Bigg|_{y_0}\varphi_2 - Gp_0 = 0, \quad (19)$$

within the ROI, a global minimization procedure was used [5], [8]–[10], [12], [18]–[21]. This numerical technique is general and applies both to linear (7) and nonlinear (19) functionals. For a given distribution $\mu(x,y)$ along the ROI boundaries, the error functional $\delta(x,y)$ must be minimized across the ROI in some general way. Here, the specific distribution $\mu_{ij} = \mu(x_i, y_j)$ is sought which minimizes the total error:

$$D = \left(\int_S \delta^2 ds\right), \quad (20)$$

where (x_i, y_j), $0 \le i \le N$, $0 \le j \le M$ is a rectangular grid covering the ROI. The integral is approximated by summing $\delta(x_i, y_i)$ over all grid points.

In discrete form, when differential and integral operators are replaced by discrete-space equivalents, simultaneous minimization of D with respect to all undetermined μ_{ij} yields a set of linear algebraic equations. In theory, therefore, reconstruction is primarily a matrix inversion. In practice, however, the matrix is poorly conditioned; it is very difficult to produce a stable inverse using noisy, experimental data. Alternatively, error minimization can be performed with an iterative approach, as discussed below.

For the nonlinear case, the unknown scalar value $p_0 = p(x_0, y_0)$ in (19) must be estimated prior to general reconstruction. This term is estimated independently by minimizing the error:

$$D_* = \left(\int_{S_*} \delta^2 ds\right) \quad (21)$$

within a thin region including the ROI boundaries, $x = x_0$ and $y = y_0$, $S_* = (x_0 \le x \le x_1, y_0 \le y \le y_M) \cup (x_0 \le x \le x_N, y_0 \le y \le y_1)$, in which the distribution of $\mu(x,y)$ is assumed known given the specified values along the boundaries themselves.

The specific iterative procedure used here to compute the distribution $\mu_{ij} = \mu(x_i, y_j)$ minimizing either (7) or (19) over the ROI is based on a gradient method

$$\mu_{ij}^{k+1} = \mu_{ij}^{k} - \lambda_{ij}^{k}\partial D/\partial\mu_{ij}, \quad (22)$$

where k is the iteration index. It starts with a trial solution $\mu(i,j)$. Then, the error D is minimized by varying the unknown shear modulus μ at only one given grid point (i,j). This procedure is repeated for each (i,j) grid point ([35], Chapter 20). The iterative parameters λ_{ij}^{k}, which determine the step size of the gradient method, were chosen based on three estimates of D. That is, the minimum of D was locally predicted using a second order polynomial approximation of D as a function of μ_{ij}^{k} at each grid point under the restriction of a decreasing error [5], [8]–[10], [12], [18]–[21], [35]. Then, a global linear predictor was used to update all λ_{ij}^{k} simultaneously. This reduced the oscillatory nature of convergence. If the total error remained nearly constant at a given step k based on the global linear predictor values, then the iterative step sizes λ_{ij}^{k} were again selected separately using the local quadratic predictor as described above. By "ping-ponging" between local and global criteria in this way, large oscillations as a function of iteration index were greatly reduced, thus speeding convergence.

All spatial derivatives in the reconstruction equations were replaced with 2nd order finite differences over the same grid (x_i, y_j). Because 2nd order finite differences use only information from neighboring pixels, error computations were optimized so that for each $\mu_{i_0 j_0}$ update, the error $\delta_{ij} = \delta(x_i, y_j)$ was computed only for $|i - i_0| \le 1$ or $|j - j_0| \le 1$. Computations continued until the total error reached a stable plateau $|D^{k+1} - D^k|/D^k < \varepsilon_0$. For all results presented below, a value of $\varepsilon_0 = 10^{-6}$ was used, and a homogeneous medium was the trial solution. It was observed that, with different displacement fields and different grid sizes, the algorithm demonstrates approximately exponential convergence. By decreasing the grid size, the rate of convergence decreased almost linearly. Typical reconstruction times on a low-end SPARC 2 workstation for the results presented below were less than 5 minutes for the nonlinear functional (19), and even less for the linear functional (7). These algorithms, however, can be further optimized for time performance, but this is beyond the scope of this paper.

III. Experimental Methods and Materials

All measurements were made with an ultrasound-based deformational imaging system similar to the one presented in [24]. A 38-mm wide, linear array transducer operating at 5 MHz was used for all studies. The array was driven with

an Ultramark-9 (ATL Corp., Bothell, WA) real-time ultrasound system operating in conventional B-scan mode. The digital radio frequency (RF) signal output by the beamformer was captured before subsequent processing and display by the Ultramark-9 back-end. By buffering RF data at the beamformer output for data capture with an external device, live images could be viewed during data capture. About 120 consecutive frames of real-time RF data were stored using a digital data capture system constructed in our lab. At a typical 35 Hz frame rate, this represents almost 4 seconds of phase sensitive ultrasound data that can be used for sensitive speckle tracking.

Measurements were made on two different gel-based phantoms. These phantoms were constructed using the procedures described in [5]–[10]. Both phantoms were 100 mm wide by 140 mm long, where all applied surface deformations were vertical, and the depth direction in the ultrasound imaging plane also was vertical. The first phantom was homogeneous and measured 117 mm in height. The second was 80 mm high and included a single cylindrical hard inclusion near the bottom of the phantom. This inclusion in the inhomogeneous phantom was 18 mm in diameter and was oriented so that the longitudinal axis of the cylinder was perpendicular to both the ultrasound image plane and the direction of the applied surface deformation. The inclusion was constructed from a higher concentration gel. This gel had a shear modulus about 2.5 times larger than the surrounding material as estimated from independent measurements of the elastic modulus using the system described in [25].

Both phantoms were vertically deformed with a 12.5 mm thick Plexiglas plate attached to a manually controlled, one-dimensional motion axis. The plate measured 125 mm by 70 mm in cross section, and almost completely covered the top surface of either phantom. Such a large plate ensured that a plane strain state was reasonably approximated for both phantoms. A hole was cut into the center to mount the imaging array. Once the array was properly secured, the bottom surface of the plate maintained continuous contact with the top surface of the phantom. Deformations were applied by smoothly turning the gear to move the plate vertically over a distance up to 30 mm during the 4 second data capture period. Consequently, very large vertical displacements could be applied during continuous ultrasound data capture.

To test both linear and nonlinear reconstruction procedures over a wide deformational range, two data sets were recorded for each phantom. Internal displacements and strains were imaged in the homogeneous phantom for applied surface displacements of 0.7 mm (0.6% average vertical strain), representing a small deformation, and 7.6 mm (6.5% average vertical strain), representing a fairly large deformation. For the phantom with a single hard inclusion, larger surface displacements were used to produce strains within the hard inclusion comparable to the average strains in the homogeneous phantom. The two data sets recorded on this phantom used a surface displacement of 2.7 mm (3.4% average vertical strain) for the small deformation case, and 12.8 mm (16% average vertical strain) for the large deformation case.

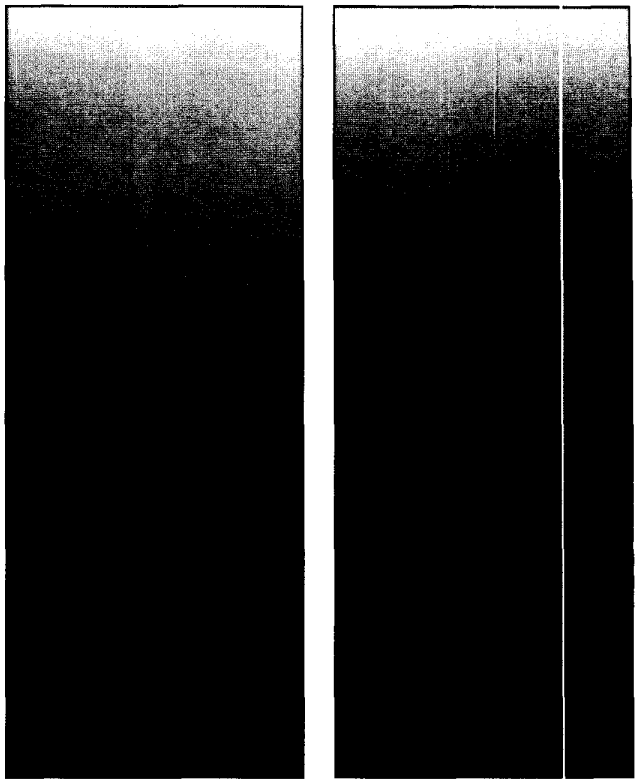

Fig. 2. Measured axial displacement images from the homogeneous phantom (left) and phantom with single hard inclusion at the bottom (right).

All displacement and strain images were computed from RF ultrasound data using the speckle tracking procedures described in [39], [40]. Based on spatial autocorrelation analysis of the axial, vertical strain image in the homogeneous phantom [39], the spatial resolution of these images was estimated to be about 1.8 mm. Consequently, the grid used for all reconstructions had equal 1.8 mm spacing in both directions (i.e., $\Delta x = \Delta y = 1.8$ mm). The shear modulus was reconstructed in all cases within a 25.1 mm × 66.4 mm rectangular ROI located near the vertical center line of the ultrasound image.

For ultrasound speckle tracking using RF data, lateral displacement estimates exhibit significantly lower SNR than axial (vertical) estimates [38]. To overcome this limitation, incompressibility processing methods have been developed for linear and nonlinear cases [37], [38]. For large deformations, the incompressibility condition is:

$$(1 + v_{,y})u_{,x} - v_{,x}u_{,y} + v_{,y} = 0. \tag{23}$$

As demonstrated in [37], the measured lateral displacement image $u^{\exp}(x, y)$ is used as a reference during lateral displacement computation. For the images presented here, the reference area was a rectangle 10.5-mm wide located near the vertical central line of the ultrasound image. In contrast with [37], where a polynomial approximation of

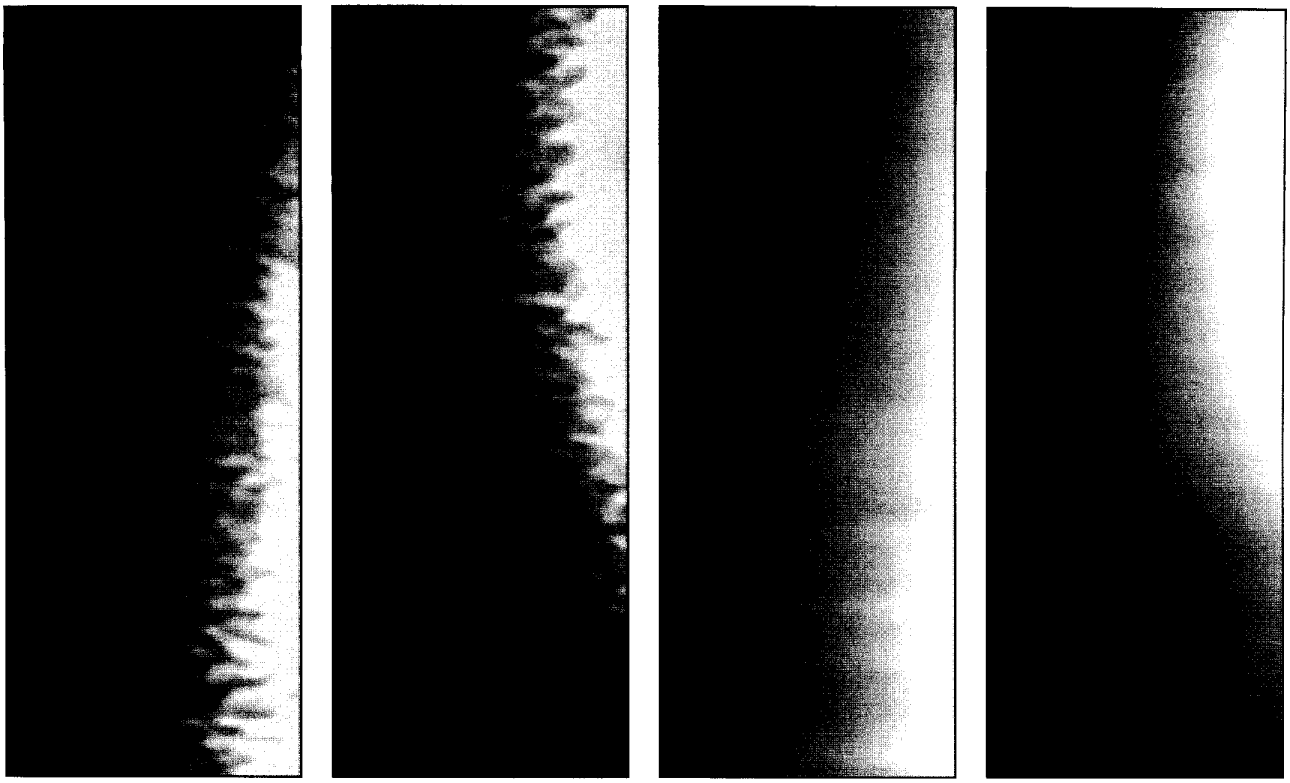

Fig. 3. Measured lateral displacements images for the homogeneous phantom (far left) and the phantom with a single hard inclusion (second from left). Incompressibility processed lateral displacement images for the homogeneous phantom (second from right) and the phantom with a single hard inclusion (far right).

the unknown lateral displacement along an entire single line yielded a solution of (23), a more flexible approach was used here; (23) was solved for a set of particular solutions of the form $u_p(x_0, y) = y^p$, $p = 1, 2, 3$ (i.e., 3rd order) within the region $y_0 - \Delta < y < y_0 + \Delta$ for every interior point (x_0, y_0). Therefore, a set of particular solutions of (23) was obtained within this region, in which the lateral displacement $u(x, y)$ is a linear combination of these particular solutions. The three unknown coefficients defining the linear combination of particular solutions were found by minimizing the total error:

$$\int_{S_R} (u - u^{\exp})^2 ds \tag{24}$$

across the corresponding area $S_R = (x_s \leq x \leq x_f, y_0 - \Delta < y < y_0 + \Delta)$ of the referenced region.

Prior to reconstruction, both measured axial displacements and incompressibility processed lateral displacements were filtered with a two-dimensional Hamming function, further reducing the spatial resolution of displacement images and subsequent elasticity reconstructions to about 2.5 mm.

IV. Results

Measured vertical (axial) displacement images over the ROI for the large deformation case are presented in Fig. 2 for the homogeneous phantom [Fig. 2(a)] and the inhomogeneous phantom [Fig. 2(b)]. In all these images the transducer, and hence the reference for all displacement measurements, is at the top. Consequently vertical displacements are zero at the top, and motion is toward the transducer (i.e., negative vertical motion). The display dynamic range for Fig. 2(a) is -5.6 mm to -0.4 mm, and for Fig. 2(b) it is -12.6 mm to -1.0 mm. Images of the measured lateral displacement are presented in Fig. 3 under the same conditions for the homogeneous phantom [Fig. 3(a)] and the inhomogeneous phantom [Fig. 3(b)]. The display dynamic range for the homogeneous phantom is -1 mm to 1 mm, and for the inhomogeneous phantom is -1 mm to 4 mm, in which black represents motion to the left and white is motion to the right. (The bottom of the phantom shifted to the right for the inhomogeneous case, and consequently an asymmetric display dynamic range is used.) Using the measured vertical displacements of Fig. 2, the same lateral displacement images after incompressibility processing are presented in Fig. 3(c) for the homogeneous phantom, and Fig. 3(d) for the inhomogeneous phantom.

Images of the shear modulus reconstructed using (7) and (19) are presented in Fig. 4 for the homogeneous phantom. Fig. 4(a) represents the linear reconstruction for the small deformation case, whereas Fig. 4(b) represents the nonlinear reconstruction. Reconstructions for the large deformation case are presented in the lower two panels,

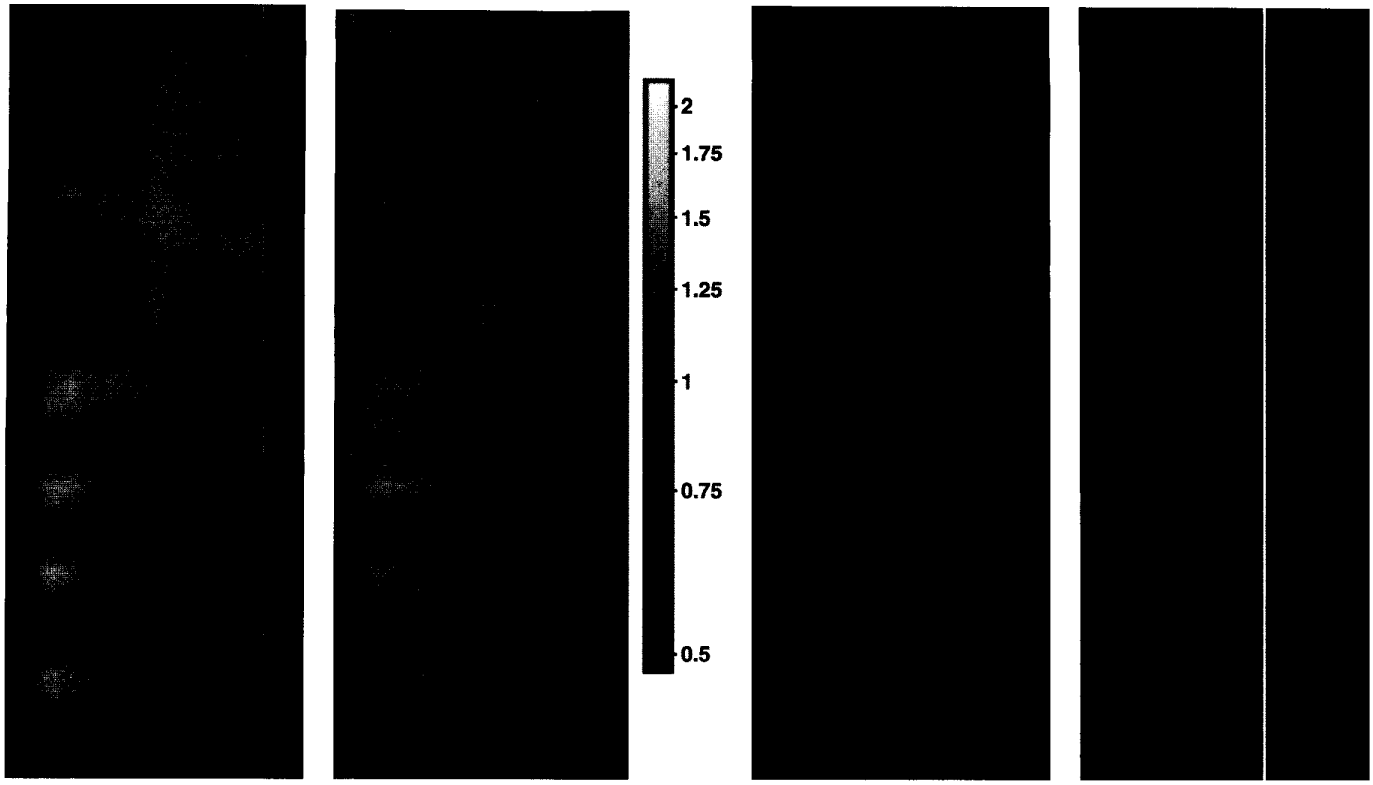

Fig. 4. Elasticity distribution for homogeneous phantom reconstructed by linear processing (far left) and (second from right), and by nonlinear processing (second from left) and (far right). Data from a 0.6% mean vertical deformation were used in (far left) and (second from left). Data from a 6.5% mean vertical deformation were used in (second from right) and (far right).

where Fig. 4(c) is the linear reconstruction and Fig. 4(d) is the nonlinear one. These relative modulus images are presented over a logarithmic gray scale (0.47 to 2.12), as illustrated on the right. The mean value of the normalized (i.e., normalized to the average elastic modulus along the boundaries of the ROI) reconstructed elasticity distribution within the ROI is 1.032 for Fig. 4(a), 1.022 for Fig. 4(c), 0.991 for Fig. 4(b) and 0.996 for Fig. 4(d). The standard deviation is 0.048 and 0.023 for Figs. 4(a) and (c), and 0.033, and 0.019 for Figs. 4(b) and (d), respectively. Artifacts in the nonlinear reconstructions are no greater than those in the linear reconstructions even for small deformations. Horizontal artifacts, created by low SNR lateral displacement measurements, are present in both linear and nonlinear reconstructions. With depth, these artifacts have more energy at lower spatial frequencies (i.e., are broader at the bottom of the image) as the lateral point spread function of the ultrasound system broadens.

Images of the shear modulus reconstructed using (7) and (19) are presented in Fig. 5 for the inhomogeneous phantom. Fig. 5(a) represents the linear reconstruction for the small deformation case, whereas Fig. 5(b) represents the nonlinear reconstruction. Reconstructions for the large deformation case are presented in the lower two panels, where Fig. 5(c) is the linear reconstruction and Fig. 5(d) is the nonlinear one. Exactly the same logarithmic gray scale as Fig. 4 was used here. Again, horizontal artifacts broaden with depth, becoming especially noticeable at the bottom of these images.

In all reconstructions, the uniform mechanical boundary condition $\mu(x, y) = 1$ was assumed along the edge of the ROI. Because the equilibrium equation is hyperbolic, any errors in this assumption produce noise across the entire reconstruction, where the relative magnitude of this noise (i.e., $|\tilde{\mu} - \mu|/\mu$ with $\tilde{\mu}$ the reconstructed image and μ the true image) is about the same as the magnitude of the boundary condition error. This analysis was confirmed by simulating numerous elasticity reconstructions of a single hard inclusion in an otherwise homogeneous medium, where boundary errors were modeled by a 10-term Fourier series with random coefficients.

The results presented in Figs. 4 and 5 demonstrate that the quality of the image reconstructed with the "geometric" nonlinear model rivals that of the reconstruction based on a linear model, even though high order displacement derivatives are used. Moreover, nonlinear processing provides more consistent elasticity reconstructions even if horizontal streak artifacts are slightly elevated compared to linear processing. To illustrate this, the elasticity distribution reconstructed along the central vertical line of the inhomogeneous phantom is presented in Fig. 6 for linear [Fig. 6(a)] and nonlinear [Fig. 6(b)] models. Clearly, nonlinear processing produces more consistent reconstructions independent of the magnitude of the external deforma-

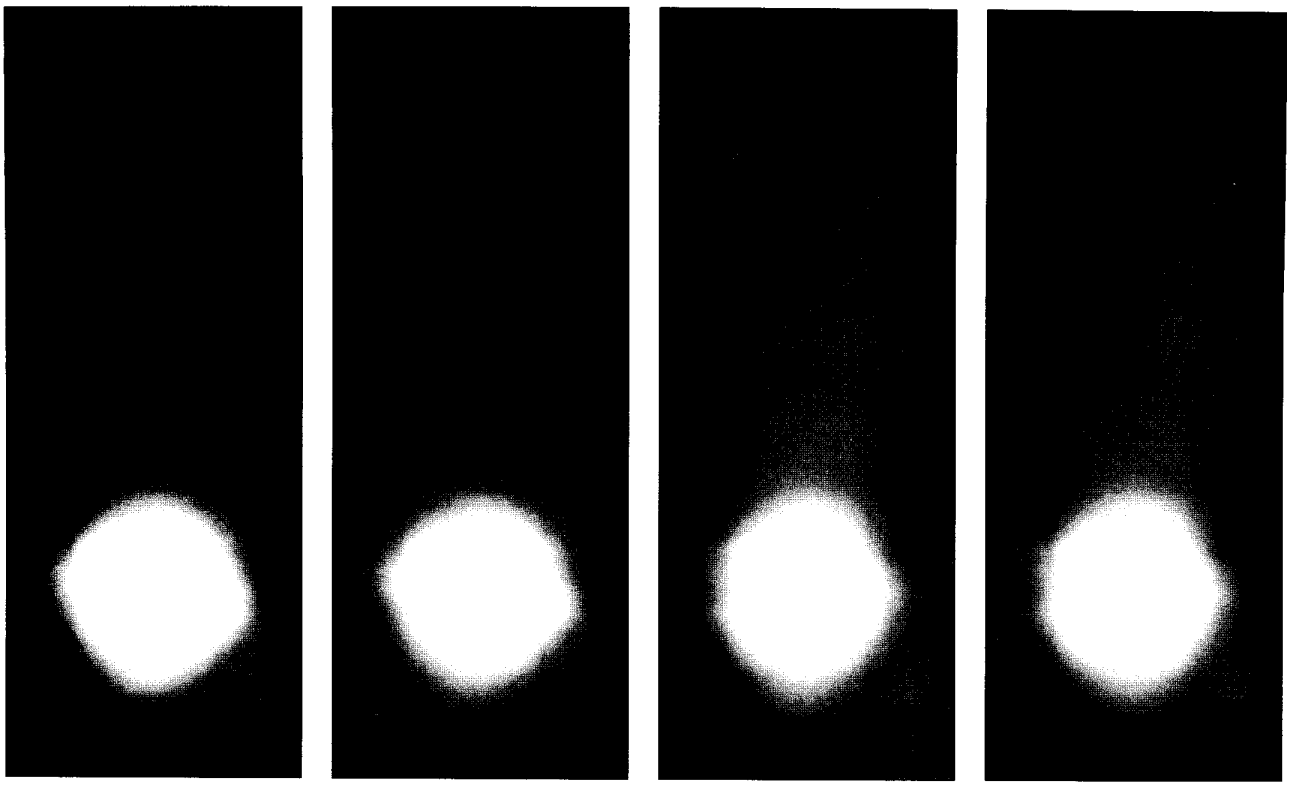

Fig. 5. Elasticity distribution for the phantom with a cylindrical hard inclusion at the bottom reconstructed by linear processing (far left) and (second from right), and nonlinear processing (second from left) and (far right). Displacement images from a 3.4% mean vertical deformation were used in (far left) and (second from left). Displacement images from a 16% mean vertical deformation were used in (second from right) and (far right).

tion. This property holds not only for single line profiles. For the homogeneous phantom, the mean squared difference between small and large deformation images computed over the entire ROI is 0.115 for the linear reconstruction [Figs. 4(a) and (c)] and 0.076 for the nonlinear reconstruction [Figs. 4(b) and (d)]. Similarly, for the inclusion phantom, the mean squared difference between small and large deformation images computed over the top half of the ROI is 0.086, and over the bottom half of the phantom it is 0.181 for the linear reconstruction [Figs. 5(a) and (c)], and 0.071 for the top half of the phantom and 0.152 for the bottom half of the nonlinear reconstruction [Figs. 5(b) and (d)].

V. Discussion

The results of elasticity reconstructions presented above show that a nonlinear (geometric) model can be used to reconstruct the shear (or Young's) elastic modulus based on internal displacement and strain fields computed from real-time ultrasound data. Despite the high order spatial derivatives of both displacement components required for this processing, the image quality of reconstructions based on a nonlinear model rival those based on a simpler, linear model. Moreover, nonlinear processing provides more consistent results so that elasticity reconstruction can be performed over a wide range of external loading.

The specific numerical methods developed here exploit an integral rather than differential representation of the elasticity equations. Given noisy displacement and strain estimates, this approach is more robust and leads to more stable reconstructions. Moreover, coupled with an iterative procedure using both local and global error predictors to accelerate convergence, it can produce shear modulus images within a few minutes on a low-end, general purpose computer. Future work will optimize software running on more powerful workstations to reduce reconstruction times to a few tens of seconds. Such times are appropriate for clinical applications using real-time ultrasound data capture and specially constructed hardware for speckle tracking.

The fundamental hypothesis of this study is that reconstruction can greatly reduce artifacts in displacement and strain images due to global boundary conditions. To illustrate this point for the specific example discussed here, the results of a simple 1-D elasticity reconstruction are presented in Fig. 7. Fig. 7 shows the normalized distribution of $1/v_{,y}$ for the homogeneous phantom [Fig. 7(a)], and the inhomogeneous phantom [Fig. 7(b)] over precisely the same display dynamic range used in Figs. 4 and 5. Because the homogeneous phantom was constructed to yield a nearly

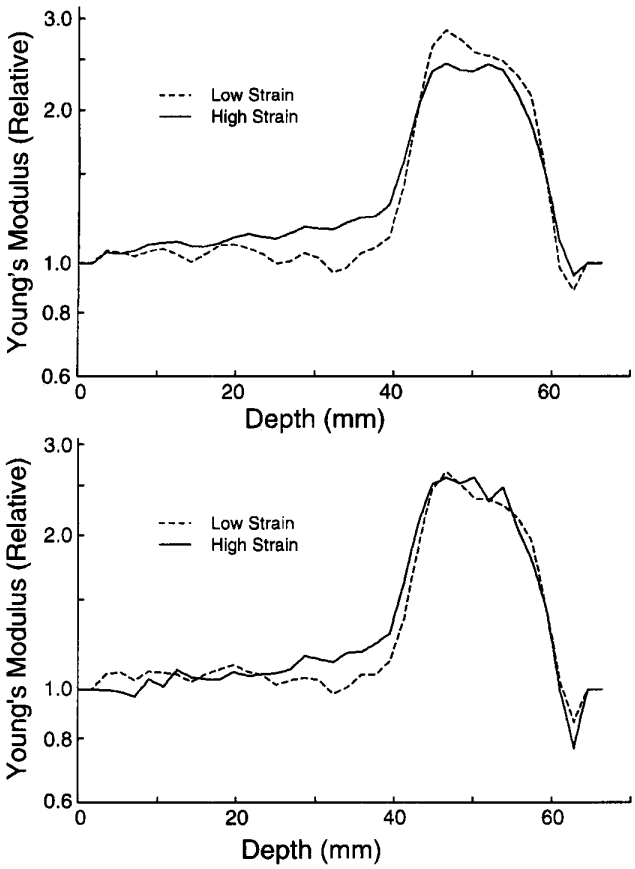

Fig. 6. Elasticity distribution along central vertical line of the inhomogeneous phantom images, reconstructed by linear (left) and nonlinear (right) processing.

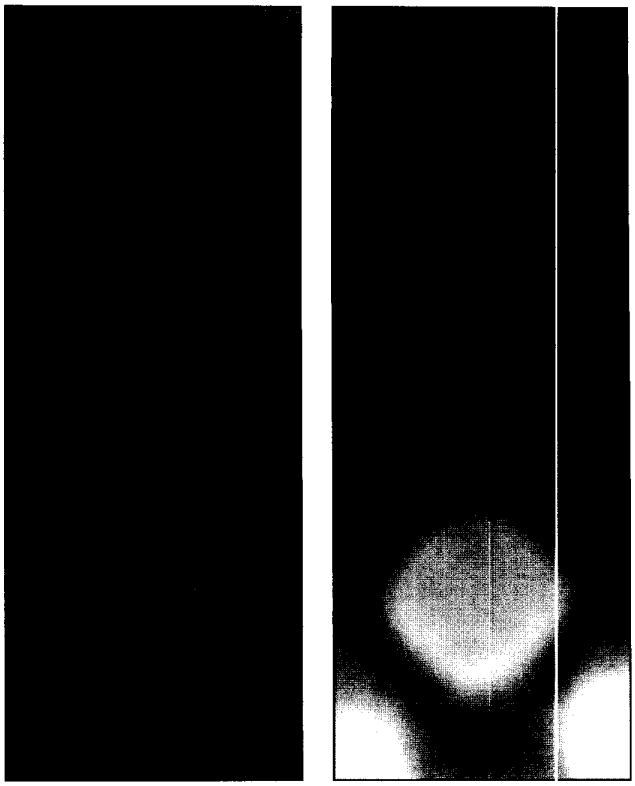

Fig. 7. Normalized distribution of $1/v_{,y}$ for the homogeneous phantom (left), and the phantom with a single hard inclusion (right).

uniform strain distribution over the ROI, the 1-D reconstruction is almost perfect. That is, measurement noise is not amplified for this type of processing, leading to a clean reconstruction. In contrast, this simple approach produces significant artifacts in images of an inhomogeneous object. Clearly, as the object becomes more complex, more accurate reconstruction is required even when uniform, one-dimensional loading is used.

All the results presented in this paper were computed assuming a linear stress-strain relation (3). This assumption is almost perfect over a wide deformation range for the gel-based, tissue-like phantoms used here [41]. Real tissue, however, exhibits nonlinear behavior (i.e., material nonlinearity) even for simple types of external loading if the deformation is significant [25], [34], [42]. Because ultrasound data can be acquired over a wide deformation range, there is the possibility that the shear modulus can be reconstructed at different strain magnitudes. Over a limited deformation range, the stress-strain curve can be considered linear, but with an elastic modulus that depends on the instantaneous strain magnitude. Displacement and strain data for an ex vivo model of kidney transplant rejection acquired over a large deformation range have been analyzed with a piecewise linear approximation to produce images related to the material nonlinearity of the kidney [24]. Future work will combine such measurements with the methods developed here to image the nonlinear elastic properties of tissue.

ACKNOWLEDGMENTS

The authors would like to thank ATL for providing the "Ultramark-9" HDI imaging system, Steve Freeman and Ramon Erkamp for designing the data acquisition hardware, and John Crowe for programming the multiprocessor control software used for displacement and strain computations.

REFERENCES

[1] T. A. Krouskop, D. R. Dougherty, and S. F. Levinson, "A pulsed Doppler ultrasonic system for making non-invasive measurements of the mechanical properties of soft tissue," *J. Rehabil. Res. Dev.*, vol. 24, no. 2, pp. 1–8, 1987.

[2] R. M. Lerner, K. J. Parker, J. Holen, R. Gramiak, and R. C. Waag, "Sono-elasticity: Medical elasticity images derived from ultrasound signals in mechanically vibrated targets," *Acoust. Imaging*, vol. 16, pp. 317–327, 1988.

[3] M. Bertrand, J. Meunier, M. Doucet, and G. Ferland, "Ultrasonic biomechanical strain gauge based on speckle tracking," *Proc. IEEE Ultrason. Symp.*, 1989, pp. 859–864.

[4] J. Ophir, I. Cespedes, H. Ponnekanti, Y. Yazdi, and X. Li, "Elastography: A quantitative method for imaging the elasticity of biological tissues," *Ultrason. Imaging*, vol. 13, pp. 111–134, 1991.

[5] M. O'Donnell, S. Y. Emelianov, A. R. Skovoroda, M. A. Lubinski, W. F. Weitzel, and R. C. Wiggins, "Quantitative elasticity imaging," *Proc. IEEE Ultrason. Symp.*, 1993, pp. 893–903.

[6] A. R. Skovoroda, S. Y. Emelianov, M. A. Lubinski, A. P. Sarvazyan, and M. O'Donnell, "Theoretical analysis and verification of ultrasound displacement and strain imaging," *IEEE Trans. Ultrason., Ferroelect., Freq. Contr.*, vol. 41, pp. 302–313, May 1994.

[7] M. O'Donnell A. R. Skovoroda, B. M. Shapo, and S. Y. Emelianov, "Internal displacement and strain imaging using ultrasonic speckle tracking," *IEEE Trans. Ultrason., Ferroelect., Freq. Contr.*, vol. 41, pp. 314–325, May 1994.

[8] S. Y. Emelianov, M. A. Lubinski, W. F. Weitzel, R. C. Wiggins, A. R. Skovoroda, and M. O'Donnell, "Elasticity imaging for early detection of renal pathologies," *Ultrason. Med. Biol.*, vol. 21, no. 7, pp. 871–883, 1995.

[9] A. R. Skovoroda, S. Y. Emelianov, and M. O'Donnell, "Tissue elasticity reconstruction based on ultrasonic displacement and strain images," *IEEE Trans. Ultrason., Ferroelect., Freq. Contr.*, vol. 42, pp. 747–765, July 1995.

[10] S. Y. Emelianov, A. R. Skovoroda, M. A. Lubinski, and M. O'Donnell, "Reconstructive elasticity imaging," *Acoust. Imaging*, vol. 21, New York: Plenum, 1995, pp. 241–252.

[11] E. I. Cespedes, Y. Huang, J. Ophir, and S. Spratt, "Method for the estimation of subsample time-delays of digitized echo signals," *Ultrason. Imaging*, vol. 17, pp. 142–171, 1995.

[12] J. B. Fowlkes, S. Y. Emelianov, J. G. Pipe, A. R. Skovoroda, R. S. Adler, P. L. Carson, and A. P. Sarvazyan, "Magnetic resonance imaging for detection of elasticity variation," *Med. Phys.*, vol. 22, no. 11, pp. 1771–1778, 1995.

[13] R. Muthupillai, D. J. Lomas, P. J. Rossman, J. F. Greenleaf, A. Manduca, and R. L. Ehman, "Magnetic resonance elastography by direct visualization of propagating acoustic strain waves," *Science*, vol. 269, pp. 1854–1857, 1995.

[14] D. B. Plewes, I. Betty, S. N. Urchuk, and I. Soutar, "Visualizing tissue compliance with MR imaging," *J. Magnetic Resonance Imaging*, vol. 5, pp. 733–738, 1995.

[15] L. Gao, K. J. Parker, R. M. Lerner, and S. F. Levinson, "Imaging of the elastic properties of tissue—A review," *Ultrason. Med. Biol.*, vol. 22, pp. 959–977, 1996.

[16] J. Ophir, I. Cespedes, B. Garra, H. Ponnekanti, Y. Huang, and N. Maklad, "Elastography: Ultrasonic imaging of tissue strain and elastic modulus in vivo," *Eur. J. Ultrasound*, vol. 3, pp. 49–70, 1996.

[17] F. Kallel and M. Bertrand, "Tissue elasticity reconstruction using linear perturbation method," *IEEE Trans. Instrum. Meas.*, vol. 15, no. 3, pp. 299–313, 1996.

[18] T. L. Chenevert, S. Y. Emelianov, and A. R. Skovoroda, "Elasticity reconstructive imaging using static displacement and strain estimation," in *Proc. Int. Soc. Magnetic Resonance in Med.*, pp. 461–462, 1997.

[19] A. R. Skovoroda, M. A. Lubinski, S. Y. Emelianov, and M. O'Donnell, "Nonlinear reconstructive elasticity imaging," *Ultrason. Imaging Tissue Characterization*, June 2–4, 1997, Arlington, VA.

[20] S. Y. Emelianov, T. L. Chenevert, A. R. Skovoroda, M. A. Lubinski, and M. O'Donnell, "Reconstructive elasticity imaging using ultrasound and NMR scanners," *Ultrason. Imaging*, vol. 19, p. 61, 1997.

[21] T. L. Chenevert, A. R. Skovoroda, M. O'Donnell, and S. Y. Emelianov, "Elasticity reconstructive imaging via stimulated echo MRI," *Magnetic Resonance Med.*, vol. 39, no. 3, pp. 482–490, 1998.

[22] C. Sumi, A. Suzuki and K. Nakayama, "Estimation of shear modulus distribution of soft tissue from strain distribution," *IEEE Trans. Biomed. Eng.*, vol. 42, no. 2, pp. 193–202, 1995.

[23] T. Varghese, J. Ophir, and E. I. Cespedes, "Noise reduction in elastography using temporal stretching with multicompression averaging," *Ultrason. Med. Biol.*, vol. 22, pp. 1043–1052, 1996.

[24] S. Y. Emelianov, M. A. Lubinski, A. R. Skovoroda, R. Q. Erkamp, S. F. Leavey, R. C. Wiggins, and M. O'Donnell, "Reconstructive ultrasound elasticity imaging for renal pathology detection," *Proc. IEEE Ultrason. Symp.*, 1997, pp. 1123–1126, Toronto, Canada, Oct. 1997.

[25] R. Q. Erkamp, P. A. Wiggins, A. R. Skovoroda, S. Y. Emelianov, and M. O'Donnell, "Measuring the elastic modulus of small tissue samples," *Ultrason. Imaging*, vol. 20, pp. 17–28, 1998.

[26] A. R. Skovoroda, *Inverse Problems of the Theory of Elasticity in the Diagnostics of Soft Tissue Pathologies*. Pushchino, Russia: Pushchino Research Center of Russian Academy of Sciences, 1992.

[27] J. E. Adkins, "Finite deformation of materials exhibiting curvilinear aeolotropy," *Proc. R. Soc. Lond. Ser. A*, vol. 229, pp. 119–134, 1955.

[28] M. A. Biot, *Mechanics of Incremental Deformations*. New York: Wiley, 1965.

[29] A. A. Ilyushin, *Mechanics of Solid Structures*. Moscow: Moscow State University Press, 1978.

[30] Y. N. Rabotnov, *Mechanics of Solid Structures*. Moscow: Nauka, 1979.

[31] M. E. Gurtin, *An Introduction to Continuum Mechanics*. New York: Academic, 1981.

[32] S. Timoshenko and J. Goodier, *Theory of Elasticity*. New York: McGraw-Hill, 1951.

[33] L. D. Landau and E. M. Lifshitz, *Theory of Elasticity*. Moscow: Nauka, 1965.

[34] F. A. Duck, *Physical Properties of Tissues*. London, England: Harcourt Brace Jovanovich, 1990.

[35] G. A. Korn and M. S. Korn, *Mathematical Handbook for Scientists and Engineers*. New York: McGraw-Hill, 1968.

[36] A. A. Samarskii and E. S. Nikolaev, *Methods of the Solution of the Net Equations*. Moscow: Nauka, 1978.

[37] A. R. Skovoroda, M. A. Lubinski, S. Y. Emelianov, and M. O'Donnell, "Nonlinear estimation of the lateral displacement using tissue incompressibility," *IEEE Trans. Ultrason., Ferroelect., Freq. Contr.*, vol. 45, no. 2, pp. 491–503, 1998.

[38] M. A. Lubinski, S. Y. Emelianov, K. R. Raghavan, A. E. Yagle, A. R. Skovoroda, and M. O'Donnell, "Lateral displacement estimation using tissue incompressibility," *IEEE Trans. Ultrason., Ferroelect., Freq. Contr.*, vol. 43, pp. 247–256, 1996.

[39] N. A. Cohn, S. Y. Emelianov, M. A. Lubinski, and M. O'Donnell, "An elasticity microscope. Part I: Methods," *IEEE Trans. Ultrason., Ferroelect., Freq. Contr.*, vol. 44, pp. 1304–1319, 1997.

[40] M. A. Lubinski, S. Y. Emelianov, and M. O'Donnell, "Speckle tracking methods for ultrasonic elasticity imaging using short time correlation," *IEEE Trans. Ultrason., Ferroelect., Freq. Contr.*, vol. 46, no. 1, pp. 82–96, 1999.

[41] T. J. Hall, M. Bilgen, M. F. Insana, and P. Chaturvedi, "Phantoms for elastography," *Proc. IEEE Ultrason. Symp.*, 1996, pp. 1193–1196.

[42] H. Demiray, "Large deformation analysis of some basic problems in biophysics," *Bull. Mathematical Biol.*, vol. 38, pp. 701–712, 1976.

APPENDIX

Assume that two displacement components are measured with high precision within the volume; also, assume that the third component is estimated less accurately, as, for example, in elasticity measurements using MRI [18], [21].

For a general three-dimensional strain state described by (1) and (3), the following system of equations analogous to (9) is produced:

$$A\nabla(p) = -pB - F, \tag{A1}$$

where

$$A(x,y) = \begin{pmatrix} 1+u_{1,1} & u_{1,2} & u_{1,3} \\ u_{2,1} & 1+u_{2,2} & u_{2,3} \\ u_{3,1} & u_{3,2} & 1+u_{3,3} \end{pmatrix},$$

$$B(x,y) = (b_i) = \nabla^2 U,$$

$$F = (f_i) = 2\left\{ A\Psi + \mu \left[\sum_{i=1}^{3} \varepsilon_{ii} U_{,ii} + \sum_{i,j=1}^{3} (1-\delta_{ij}) \varepsilon_{ij} U_{,ij} \right] \right\},$$

$$\Psi = (\psi_i) = (\mu\varepsilon_{1i})_{,1} + (\mu\varepsilon_{2i})_{,2} + (\mu\varepsilon_{3i})_{,3}, \quad i = 1,2,3;$$

$$\nabla = (\partial/\partial x_1, \partial/\partial x_2, \partial/\partial x_3),$$

$$\nabla^2 = \partial^2/\partial x_1^2 + \partial^2/\partial x_2^2 + \partial^2/\partial x_3^2.$$

Note that the nonlinear form of the strain tensor (10) must be used.

To solve (A1) with respect to unknowns $\partial p/\partial x_1$, $\partial p/\partial x_2$, and $\partial p/\partial x_3$, we first compute the determinant of matrix A, which is

$$\det(A) = 1 + DivU + \det\begin{pmatrix} u_{,x} & u_{,y} \\ v_{,x} & v_{,y} \end{pmatrix} + \det\begin{pmatrix} v_{,y} & v_{,z} \\ w_{,y} & w_{,z} \end{pmatrix} + \det\begin{pmatrix} u_{,x} & u_{,z} \\ w_{,x} & w_{,z} \end{pmatrix} + \det\begin{pmatrix} u_{,x} & u_{,y} & u_{,z} \\ v_{,x} & v_{,y} & v_{,z} \\ w_{,x} & w_{,y} & w_{,z} \end{pmatrix} = \sqrt{g},$$

where $g = \det(g_{ij})$ is the determinant of the 2nd ranked metric tensor g_{ij}.

Note that for incompressible materials $g = 1$, and, $\det(A) = 1$ which greatly simplifies the inversion of (A1):

$$\nabla(p) = \alpha p + \beta, \tag{A2}$$

where $\alpha(x,y) = (\alpha_i) = -A^{-1}B$, $\beta(x,y) = (\beta_i) = -A^{-1}F$, $i = 1,2,3$.

By integrating each component equation of (A2) along its corresponding coordinate, we obtain:

$$\begin{aligned} p(x_1,x_2,x_3) &= \varphi_1 p(x_1^0,x_2,x_3) + F_1 \\ &= \varphi_2 p(x_1,x_2^0,x_3) + F_2 \\ &= \varphi_3 p(x_1,x_2,x_3^0) + F_3 \end{aligned} \tag{A3}$$

where

$$\varphi_i(x_1,x_2,x_3) = \exp\left[\int_{x_i^0}^{x_i} \alpha_i(x_1,x_2,x_3) dx_i \right],$$

$$F_i(x_1,x_2,x_3) = \left(\int_{x_i^0}^{x_i} \frac{\beta_i}{\varphi_i} dx_i \right) \varphi_i, \quad i = 1,2,3.$$

Using a procedure paralleling that used to produce (14), the three-dimensional case reduces to:

$$\begin{aligned} &[(\varphi_2\varphi_3|_{x_2^0} + \varphi_3\varphi_2|_{x_3^0})p_0 + (\varphi_2 F_3|_{x_2^0} + \varphi_3 F_2|_{x_3^0}) \\ &\qquad + (F_2 + F_3)]|_{x_1^0}\varphi_1 + 2F_1 = \\ &[(\varphi_1\varphi_3|_{x_1^0} + \varphi_3\varphi_1|_{x_3^0})p_0 + (\varphi_1 F_3|_{x_1^0} + \varphi_3 F_1|_{x_3^0}) \\ &\qquad + (F_1 + F_3)]|_{x_2^0}\varphi_2 + 2F_2 = \\ &[(\varphi_1\varphi_2|_{x_1^0} + \varphi_2\varphi_1|_{x_2^0})p_0 + (\varphi_1 F_2|_{x_1^0} + \varphi_2 F_1|_{x_2^0}) \\ &\qquad + (F_1 + F_2)]|_{x_3^0}\varphi_3 - 2F_3, \end{aligned} \tag{A4}$$

where $p_0 = p(x_1^0, x_2^0, x_3^0)$. For a plane strain state (A4) reduces to (14).

Again, in the limit of small displacements, $\alpha = 0$, $\varphi_i = 1$, $i = 1,2,3$, (A4) can be greatly simplified:

$$\begin{aligned} &(F_3|_{x_2^0} + F_2|_{x_3^0} + F_2 + F_3)|_{x_1^0} + 2F_1 = \\ &\qquad (F_3|_{x_1^0} + F_1|_{x_3^0} + F_1 + F_3)|_{x_2^0} + 2F_2 = \\ &\qquad\qquad (F_2|_{x_1^0} + F_1|_{x_2^0} + F_1 + F_2)|_{x_3^0} + 2F_3, \end{aligned} \tag{A5}$$

where

$$F_1 = 2\left\{ (\mu\varepsilon_{11})|_{x_1^0} - \mu\varepsilon_{11} - \int_{x_1^0}^{x_1} [(\mu\varepsilon_{12})_{,2} - (\mu\varepsilon_{13})_{,3}] dx_1 \right\},$$

$$F_2 = 2\left\{ (\mu\varepsilon_{22})|_{x_2^0} - \mu\varepsilon_{22} - \int_{x_2^0}^{x_2} [(\mu\varepsilon_{12})_{,1} - (\mu\varepsilon_{23})_{,3}] dx_2 \right\},$$

$$F_3 = 2\left\{ (\mu\varepsilon_{33})|_{x_3^0} - \mu\varepsilon_{33} - \int_{x_3^0}^{x_3} [(\mu\varepsilon_{13})_{,1} - (\mu\varepsilon_{23})_{,2}] dx_3 \right\}.$$

Equations (A4) and (A5) do not contain high order spatial displacement derivatives, compared with their equivalent differential equations, and therefore, elasticity reconstruction by (A4) and (A5) should be more stable. Again, (A4) and (A5) show that spatial derivatives of all displacement components are needed in general for elasticity reconstruction in both linear and nonlinear cases, but any one of the three displacement components can be reconstructed using incompressibility processing based on the relation ($\det(A) = 1$) [37].

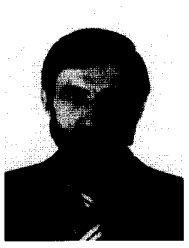

Andrei R. Skovoroda received the B.S. and M.S. degrees in mathematics and mechanics in 1973 and 1975, respectively, from the Novosibirsk State University, USSR, and the Ph.D. degree in 1985 from the Moscow State University, USSR.

From 1975 to 1977 he was a lecturer in theoretical mechanics at the College of Textile Technology, Barnaul, USSR. From 1977 to 1980 he was a Ph.D. researcher at the subfaculty of Plasticity of the Moscow State University, where he worked on the dynamic behavior of plates under blast-type loading. In 1981 he held an appointment as a junior research associate at the Laboratory of Mathematical Modeling of the Research Computing Center of the USSR Academy

of Sciences (the present name: Institute of Mathematical Problems of Biology, Russian Academy of Sciences), where he developed efficient mathematical methods to solve the differential equations of the theory of elasticity. In 1986 he became a senior research associate and was scientific secretary at the same institute from 1988 to 1993. He is currently head of the Laboratory of Mathematical Problems in Biomechanics and works on the biomechanics of soft tissue.

Dr. Skovoroda has authored and co-authored more than 80 articles for archival publications and papers presented at all-union and international meetings.

Mark A. Lubinski (S'94) received the B.S. degree in electrical engineering (with biomedical engineering option) in 1990 from Carnegie Mellon University and the M.S. in bioengineering and electrical engineering (systems) in 1993 and 1994, respectively, from the University of Michigan, Ann Arbor.

Before beginning his graduate work, he worked as a computer engineer in the Department of Neurophysiology at the Children's Hospital of Pittsburgh. While at the University of Michigan he was a National Science Foundation Graduate Fellow in Bioengineering and a GAANN Fellow. He is currently a graduate student research assistant at the University of Michigan, working in the Biomedical Ultrasonics Laboratory, pursuing a Ph.D. in biomedical engineering, and researching ultrasonic elasticity imaging. He is a member of Tau Beta Pi and Eta Kappa Nu. His research interests include signal processing, medical imaging, and motion estimation.

Stanislav Y. Emelianov (M'94) was born in May 1966. He received the B.S. and M.S. degrees in physics in 1986 and 1989, respectively, from Moscow State University, and the Institute of Mathematical Problems of Biology of the Russian Academy of Sciences, Russia.

In 1989, he joined the Institute of Mathematical Problems of Biology, where he was engaged in both mathematical modeling of soft tissue biomechanics and experimental studies of noninvasive methods in medical diagnostics based on tissue elasticity variations. Following his graduate work, he moved to the University of Michigan, Ann Arbor, as a post-doctoral fellow in the Electrical Engineering and Computer Science Department working on applications of imaging systems for medical diagnosis and nondestructive testing. Dr. Emelianov is currently a research scientist in the Biomedical Ultrasonics Laboratory at the University of Michigan and involved primarily in the theoretical and practical aspects of ultrasound elasticity imaging. He is the author of several scientific papers. His research interests are in the areas of tissue biomechanics, medical imaging systems, and nondestructive material testing.

Matthew O'Donnell (M'79–SM'84–F'93) received the B.S. and Ph.D. degrees in physics from the University of Notre Dame, Notre Dame, IN, 1972 and 1976, respectively.

Following his graduate work, he moved to Washington University in St. Louis as a postdoctoral fellow in the Physics Department working on applications of ultrasonics to medicine and non-destructive testing. He subsequently held a joint appointment as a Senior Research Associate in the Physics Department and a Research Instructor of Medicine in the Department of Medicine at Washington University. In 1980 he moved to General Electric Corporate Research and Development in Schenectady, New York, where he continued to work on medical electronics, including NMR and ultrasound imaging systems. During the 1984–1985 academic year, he was a visiting fellow in the Department of Electrical Engineering at Yale University investigating automated image analysis systems. Most recently, he has worked on the application of advanced VLSI circuits to medical imaging systems, including catheter arrays. In a bold move during 1990, Dr. O'Donnell moved to the Electrical Engineering & Computer Science Department at the University of Michigan in Ann Arbor, Michigan, where he is currently a Professor.

Dr. O'Donnell is a member of Sigma Xi, the American Physical Society, and is a fellow of both the IEEE and the AIMBE. He has authored or coauthored over 100 archival publications, including 2 receiving best paper awards, numerous presentations at national meetings, and 40 patents.